TASK 7 DEMONSTRATION OF THAMES FOR MICROSTRUCTURE AND TRANSPORT PROPERTIES

Cementitious Barriers Partnership

March 2010

CBP-TR-2010-007-C2, Rev. 0

CEMENTITIOUS BARRIERS PARTNERSHIP TASK 7 DEMONSTRATION OF THAMES FOR MICROSTRUCTURE AND TRANSPORT PROPERTIES

J. W. Bullard, P. E. Stutzman, K. A. Snyder, and E. J. Garboczi
National Institute of Standards and Technology
Materials and Construction Research Division
Gaithersburg, MD 20899

March 2010

CBP-TR-2010-007-C2, Rev. 0

ACKNOWLEDGEMENTS

This report was prepared for the United States Department of Energy under Interagency Agreement No. DE-AI09-09SR22667 and is an account of work performed under that contract. Reference herein to any specific commercial product, process, or service by trademark, name, manufacturer, or otherwise does not necessarily constitute or imply endorsement, recommendation, or favoring of same by Savannah River Nuclear Solutions or by the United States Government or any agency thereof. The views and opinions of the authors expressed herein do not necessarily state or reflect those of the United States Government or any agency thereof. This report is part of a larger multi-investigator project supported by the U. S. Department of Energy entitled the Cementitious Barriers Partnership. The opinions, findings, conclusions, or recommendations expressed herein are those of the authors and do not necessarily represent the views of the U.S. Department of Energy. This work was also partially supported by the National Institute of Standards and Technology Sustainable Concrete Materials program.

DISCLAIMER

This work was prepared under an agreement with and funded by the U. S. Government. Neither the U.S. Government or its employees, nor any of its contractors, subcontractors or their employees, makes any express or implied: 1. warranty or assumes any legal liability for the accuracy, completeness, or for the use or results of such use of any information, product, or process disclosed; or 2. representation that such use or results of such use would not infringe privately owned rights; or 3. endorsement or recommendation of any specifically identified commercial product, process, or service. Any views and opinions of authors expressed in this work do not necessarily state or reflect those of the United States Government, or its contractors, or subcontractors, or subcontractors.

Printed in the United States of America

United States Department of Energy
Office of Environmental Management
Washington, DC

This document is available on the U.S. DOE Information Bridge and on the CBP website: http://cementbarriers.org/
An electronic copy of this document is also available through links on the following website: http://srnl.doe.gov/

FOREWORD

The Cementitious Barriers Partnership (CBP) Project is a multi-disciplinary, multi-institutional collaboration supported by the United States Department of Energy (US DOE) Office of Waste Processing. The objective of the CBP project is to develop a set of tools to improve understanding and prediction of the long-term structural, hydraulic, and chemical performance of cementitious barriers used in nuclear applications.

A multi-disciplinary partnership of federal, academic, private sector, and international expertise has been formed to accomplish the project objective. In addition to the US DOE, the CBP partners are the Savannah River National Laboratory (SRNL), Vanderbilt University (VU) / Consortium for Risk Evaluation with Stakeholder Participation (CRESP), Energy Research Center of the Netherlands (ECN), and SIMCO Technologies, Inc. The Nuclear Regulatory Commission (NRC) is providing support under a Memorandum of Understanding. The National Institute of Standards and Technology (NIST) is providing research under an Interagency Agreement. Neither the NRC nor NIST are signatories to the CRADA.

The periods of cementitious performance being evaluated are >100 years for operating facilities and > 1000 years for waste management. The set of simulation tools and data developed under this project will be used to evaluate and predict the behavior of cementitious barriers used in near-surface engineered waste disposal systems, e.g., waste forms, containment structures, entombments, and environmental remediation, including decontamination and decommissioning analysis of structural concrete components of nuclear facilities (spent-fuel pools, dry spent-fuel storage units, and recycling facilities such as fuel fabrication, separations processes). Simulation parameters will be obtained from prior literature and will be experimentally measured under this project, as necessary, to demonstrate application of the simulation tools for three prototype applications (waste form in concrete vault, high-level waste tank grouting, and spent-fuel pool). Test methods and data needs to support use of the simulation tools for future applications will be defined.

The CBP project is a five-year effort focused on reducing the uncertainties of current methodologies for assessing cementitious barrier performance and increasing the consistency and transparency of the assessment process. The results of this project will enable improved risk-informed, performance-based decision-making and support several of the strategic initiatives in the DOE Office of Environmental Management Engineering & Technology Roadmap. Those strategic initiatives include 1) enhanced tank closure processes; 2) enhanced stabilization technologies; 3) advanced predictive capabilities; 4) enhanced remediation methods; 5) adapted technologies for site-specific and complex-wide D&D applications; 6) improved SNF storage, stabilization and disposal preparation; 7) enhanced storage, monitoring and stabilization systems; and 8) enhanced long-term performance evaluation and monitoring.

Christine A. Langton, PhD
Savannah River National Laboratory

David S. Kosson, PhD
Vanderbilt University / CRESP

EXECUTIVE SUMMARY

The goal of the Cementitious Barriers Partnership (CBP) is to develop a reasonable and credible set of tools to reduce the uncertainty in predicting the structural, hydraulic and chemical performance of cement barriers used in nuclear applications that are exposed to dynamic environmental conditions over extended time frames.

One of these tools, the responsibility of NIST, is THAMES (**T**hermodynamic **H**ydration **A**nd **M**icrostructure **E**volution **S**imulator), which is being developed to describe cementitious binder microstructures and calculate important engineering properties during hydration and degradation.

THAMES is designed to be a "micro-probe", used to evaluate changes in microstructure and properties occurring over time because of hydration or degradation reactions in a volume of about 0.001 mm^3. It will be used to map out microstructural and property changes across reaction fronts, for example, with spatial resolution adequate to be input into other models (e.g., STADIUM®, LeachXS™) in the integrated CBP package.

THAMES leverages thermodynamic predictions of equilibrium phase assemblages in aqueous geochemical systems to estimate 3-D virtual microstructures of a cementitious binder at different times during the hydration process or potentially during degradation phenomena. These virtual microstructures can then be used to calculate important engineering properties of a concrete made from that binder at prescribed times. In this way, the THAMES model provides a way to calculate the time evolution of important material properties such as elastic stiffness, compressive strength, diffusivity, and permeability. Without this model, there would be no way to update microstructure and properties for the barrier materials considered as they are exposed to the environment, thus greatly increasing the uncertainty of long-term transport predictions.

This Task 7 report demonstrates the current capabilities of THAMES. At the start of the CBP project, THAMES did not exist, so that it is in the early stages of development. However, extensive experience with 3-D microstructure models at NIST is making possible a timely development process.

CONTENTS

ACKNOWLEDGEMENTS ..... **II**
DISCLAIMER ..... **II**
FOREWORD ..... **III**
EXECUTIVE SUMMARY ..... **IV**
LIST OF FIGURES ..... **VI**
LIST OF TABLES ..... **VI**
LIST OF SYMBOLS ..... **VII**
LIST OF ACRONYMS AND ABBREVIATIONS ..... **VIII**
1.0 INTRODUCTION **1**
2,0 BACKGROUND AND STRUCTURE OF THE REPORT **2**
3.0 MATERIALS AND METHODS **4**
3.1 Particle Size Distribution 4
3.2 Cement Powder Image Processing and Phase Analysis 5
3.3 Stereological Analysis 5
3.4 Tracking Hydration and Microstructure Development 6
3.5 Cement Particle Shape Characterization 9
4.0 MODELING APPROACH **9**
4.1 Thermodynamic Calculations 9
4.2 Reaction Rates of Cement Clinker Phases 10
4.3 Microstructure Modeling 10
5.0 RESULTS **13**
5.1 Bulk Phases 13
5.2 Heat of Hydration and Compressive Strength 15
5.3 Microstructure Development 16
6.0 MAKING PREDICTIONS AT THE MORTAR AND CONCRETE LENGTH SCALES (CONCPROPS) **19**
7.0 DISCUSSION **20**
8.0 SUMMARY AND PROSPECTUS **21**
9.0 REFERENCES **21**

LIST OF FIGURES

Figure 1. Generic depiction of relative rates of dissolution and precipitation in a hydrating cement paste 3

Figure 2. Particle size distributions, plotted as probability density functions, measured for cements CCRL 151 and CCRL 168 using laser diffraction from a dilute suspension of particles in isopropyl alcohol. 4

Figure 3. Final processed images of (a) CCRL 151 and (b) CCRL 168 6

Figure 4. Mass fractions of the four major clinker phases, C–S–H gel, CH, ettringite, and monosulfate as a function of time in CCRL 151 paste (w/c = 0.45) hydrated at 23 °C under sealed conditions 13

Figure 5. Mass fractions of the four major clinker phases, C–S–H gel, CH, ettringite, and monosulfate as a function of time in CCRL 168 paste (w/c = 0.45) hydrated at 23 °C under sealed conditions 14

Figure 6. Predicted time dependence of the heat release in CCRL 151 and CCRL 168 pastes (w/c = 0.40) cured under sealed conditions at 23 °C 16

Figure 7. Predicted time dependence of the compressive strength in CCRL 151 and CCRL 168 mortars (w/c = 0.485) cured under sealed conditions at 23 °C 16

Figure 8. SEM images of polished sections of CCRL 168 paste hydrated for 7 d at 23 °C under sealed conditions 17

Figure 9. Slices of the simulated microstructure of CCRL 168 paste hydrated for 7 d at 23 °C under sealed conditions 18

Figure 10. Two-point correlation functions as a function of distance, r, normalized by their values at r = 0, for the simulated hydration of CCRL 168 with w/c = 0.45, including capillary porosity, unhydrated cement grains, CH, and combined ettringite (AFt) and monosulfate (AFm) phases 19

LIST OF TABLES

Table 1. Major oxide components for CCRL 151 and CCRL 168 as measured by approximately 250 laboratories, reported as mass per cent 7

Table 2. Phase composition, in mass per cent of major phases in CCRL 151 and CCRL 168, based on Rietveld refinement of X-ray powder diffraction patterns using 11 % corundum by mass as an internal standard 8

Table 3. Interphase affinities, random growth probabilities, and nucleation probabilities assumed in the simulations 12

LIST OF SYMBOLS

$\{D\}_m$	"Dissolution site" list
$\{G\}_m$	"Growth site" list
ϕ	Volume fraction of a phase in a microstructure
$I_p(x,y)$	Array designating if the pixel at location (x,y) contains the phase or phases designated by p
m	index designating a solid phase
N_m	Net number of voxels of each phase m
R_d	Uptake distribution ratio in ml/g
σ	Mortar cube compressive strength
$S_p(x,y)$	Two-point correlation function for a phase or collection of phases designated by p
V_i	Particle volume
X	Powers gel-space ratio

LIST OF ACRONYMS AND ABBREVIATIONS

BE	Backscattered electron
CBP	Cementitious Barriers Partnership
CCRL	Cement and Concrete Reference Laboratory
CRESP	Consortium for Risk Evaluation with Stakeholder Participation
CT	Computed tomography
ECN	Energy Research Centre of the Netherlands
NIST	National Institute of Standards and Technology
NRC	Nuclear Regulatory Commission
OPC	Ordinary portland cement
PLC	Portland-limestone cement
PSD	Particle size distributions
QXRD	Quantitative X-ray powder diffraction
SCM	Supplementary cementitious materials
SEM	Scanning electron microscopy
SH	Spherical harmonic
SRPC	Sulfate-resisting portland cement
TGA	Thermogravimetric
THAMES	Thermodynamic Hydration And Microstructure Evolution Simulator
VCCTL	Virtual Cement and Concrete Testing Laboratory
w/c	Water-to-cement mass ratio
XR	X-ray

Cementitious Barriers Partnership Task 7 Demonstration of THAMES for Microstructure and Transport Properties

J.W. Bullard, P.E. Stutzman, K.A. Snyder, and E.J. Garboczi
National Institute of Standards and Technology
Materials and Contruction Research Division
Gaithersburg, MD 20899

1.0 INTRODUCTION

The goal of the Cementitious Barriers Partnership (CBP) is to develop a reasonable and credible set of tools to predict the structural, hydraulic and chemical performance of cement barriers used in nuclear applications over extended time frames (e.g., >100 years for operating facilities and >1000 years for waste management). The simulation tools will be used to evaluate and predict the behavior of cementitious barriers used in near surface engineered waste disposal systems including waste forms, containment structures, entombments and environmental remediation. These cementitious materials are exposed to dynamic environmental conditions that cause changes in material properties via aging, chloride attack, sulfate attack, carbonation, oxidation, and primary constituent leaching.

A set of state-of-the-art software tools has been selected as a starting point to capture these critical aging and degradation phenomena. Through the CBP, computational tools will be developed or modified to improve the assessment of long-term structural, hydraulic, and chemical performance of cementitious materials. One of these tools, the responsibility of NIST, is THAMES (**T**hermodynamic **H**ydration **A**nd **M**icrostructure **E**volution **S**imulator), which is being developed to describe cementitious binder microstructures and calculate important engineering properties during hydration and degradation.

THAMES leverages thermodynamic predictions of equilibrium phase assemblages in aqueous geochemical systems to estimate 3-D virtual microstructures of a cementitious binder at different times during the hydration process or potentially during degradation phenomena. These virtual microstructures can then be used to calculate important engineering properties of a concrete made from that binder at prescribed times. In this way, the THAMES model provides a way to calculate the time evolution of important material properties such as elastic stiffness, compressive strength, effective DC conductivity, and permeability.

THAMES is designed to be a micro-scale model to compute the microstructure and properties at a given point in a cement-based material. It can be thought of as a "micro-probe", used to evaluate changes in microstructure and properties in a volume less than a cubic millimeter that arise from hydration or degradation reactions. Because of this, any demonstration of current THAMES capabilities will not directly address the length scale and geometry of the four DOE-CBP test cases, since that is not what THAMES is being designed to do. THAMES is a material model, not a structural model – not a limitation but a classification – so that THAMES is designed to provide key material properties to structural models. In this Task 7 report, the current capabilities of THAMES will be demonstrated. Note that at the start of the CBP project, THAMES did not exist, so that it is in the early stages of development. However, extensive experience with 3-D microstructure models is making a timely development process possible for THAMES. The Task 10 research plan describes the many improvements to the model that will need to be developed, over a period of several years, starting in FY2010.

The structure of the THAMES software is as follows. This reminder will help put this report into perspective. THAMES is composed of four modules. **GENMIC** is the module that prepares the initial particle microstructure (at the cement paste level) for the as-mixed cementitious system. **GEMS** is the thermodynamic

engine, supported by the cemdata07 thermodynamic database that gives predictions of the type and amount of phases that are formed through chemical processes. **EVOLVER** is the module that takes the thermodynamic data on the nature and amount of chemical phases present in the cementitious system and uses these data to construct a 3-D digital microstructure. Finally, **CONCPROPS** is the module that computes the physical properties of the hydrated/degraded cementitious system and uses various scaling methods to compute the accompanying mortar and concrete properties.

The current capabilities of THAMES are limited to computation of the hydration and resulting microstructure of portland cement paste with extensions to portland cement concrete. A complete mineralogical and physical description of the starting cements used for this demonstration will also be given. Experimental data on the two cements used in this demonstration will include the following time-dependent properties: degree of hydration, phase mass fractions, pore solution composition, porosity, quantitative microstructure in 3-D (e.g., tortuosity, pore connectivity, percolation, correlation functions, and simulated micrographs of the cement paste microstructure at various ages), heat output for isothermal conditions, and predictions of 28-day compressive strength vs. experiment. Other predictions, not described in detail in this report, include linear elastic moduli vs. time and computations of relative ionic diffusivity (formation factor) vs. time. The report will conclude by discussing predictions at the concrete scale – e.g., elastic moduli, ITZ microstructure and its effect on transport properties, and discussion of how THAMES might be used for fluid permeability.

2.0 BACKGROUND AND STRUCTURE OF THE REPORT

The hydration of cement paste is an inherently non-equilibrium process. When mixed with water, the thermodynamic driving force for dissolution of clinker phases is large, on the order of kJ per mole of alite (the impure C_3S clinker phase), and several tens of kJ per mole of C_3A[1]. The overall hydration reaction in portland cement can release about 100 J of heat per gram of solid within the first several minutes after mixing. Moreover, at least one of the important solid products of hydration, C–S–H gel, precipitates with no long-range crystalline order and, therefore, cannot be in its lowest free energy state. Therefore, one would expect equilibrium thermodynamic considerations to have little relevance to the course of cement paste hydration and microstructure development.

However, within several hours after mixing, the rates of the hydration reactions decrease considerably and continue to decrease with time. In addition, most of the solid products of hydration that exist in mature cement paste have nucleated and are present in significant quantities by this time. At these later times, the dissolution rates of initial cement phases decreases significantly because they have less surface area remaining and because that surface can be partially covered with hydration products such as C–S–H gel and ettringite. The hydration products, however, remain in intimate contact with the pore solution and their surface areas continue to grow. Therefore, one is able to assume at later ages that the assemblage of hydration products is nearly in equilibrium with the pore solution (see Figure 1). Under this assumption, continued microstructure development is viewed as a sequence of quasi-static changes from one microstructure state to another as the slow dissolution of initial cement phases causes infinitesimal perturbations to the pore solution composition.

The assumption of near equilibrium conditions between the assemblage of hydration products and pore solution implies that the assemblage is chemically isolated at any given time, with the overall elemental composition determined by the dissolved mass of each initial cement phase up to that time. Minimizing the free energy leads to predictions of the equilibrium mass fraction and composition of each hydrated product phase, as well as the composition and speciation of the pore solution. The power of this approach depends on having a fairly comprehensive database of thermodynamic properties of each of the condensed phases and solute species that can possibly be present. These properties include the Gibbs free energy of formation, molecular mass, density, and temperature-dependent heat capacity.

[1] Where it is convenient and not likely to cause confusion, conventional cement chemistry notation is used, i.e. C = CaO, S = SiO_2, A = Al_2O_3, F = Fe_2O_3, $\bar{S}$ = SO_3, and H = H_2O.

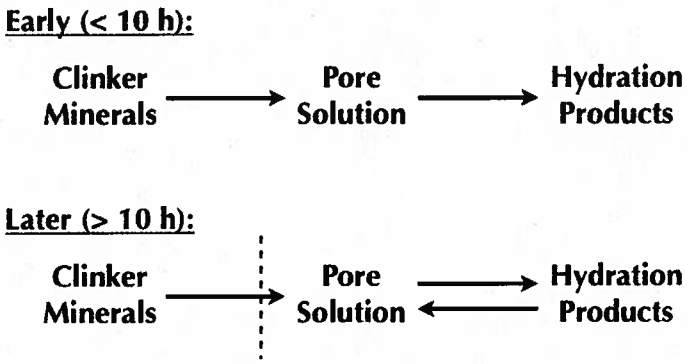

Figure 1. Generic depiction of relative rates of dissolution and precipitation in a hydrating cement paste. At early ages, dissolution of clinker phases is rapid and growth of hydration products is comparable. At later ages, the surface area of clinker phases decreases and may be partially obstructed by coverage of hydration products. Under these conditions, the pore solution and hydrated product assemblage may approach near-equilibrium conditions.

Although this approach is primarily thermodynamic, it still requires some kind of kinetic model to predict the dissolved mass of initial cement phases as a function of time. The rate of dissolution of cement phases, even at later times, should depend on temperature and on microstructural characteristics such as the specific surface area of each cement phase and the water-to-cement mass ratio (w/c). Lothenbach and Winnefeld (2006) and Lothenbach and Wieland (2006) have identified an empirical kinetic model of clinker phase dissolution (Parrott & Killoh 1984) for this purpose, and have coupled it to a Gibbs free energy minimization program called GEMS (Kulik 2009) to model the time dependence of the phase assemblage and pore solution composition in pastes of ordinary portland cement (OPC) (Lothenbach & Winnefeld 2006) and sulfate-resisting portland cement (SRPC) (Lothenbach & Wieland 2006). They reported both pore solution speciation and mass fractions of each phase as a function of time out to 1.1 years of hydration for OPC pastes with or without limestone additions at 20 °C. The same modeling tools have been used to simulate the influence of curing temperature (Lothenbach et al. 2008b) and limestone additions (Lothenbach et al. 2008a) on the hydration kinetics and porosity of pastes of OPC, SRPC and portland-limestone cement (PLC). Guillon, Chen, and Chanvillard (2008) used a different thermodynamic database (Guillon 2004) with the thermodynamic speciation software PHREEQC (Parkhurst & Appelo 1999), and coupled it to a kinetic model of OPC hydration by Tomosawa (1997) to predict the rate of cement hydration and time dependence of the mass fractions of hydrated phases in an OPC.

One aspect that is not present in these recent thermodynamic approaches is a model of the spatial distribution of phases, i.e. microstructure, as a function of time. Microstructure is not a thermodynamic property because the free energy of any phase is translationally and rotationally invariant. Even if the excess free energy of the various kinds of interphase boundaries were taken into account, minimization of free energy requires minimization of the boundary areas, which is accomplished only when each phase is present as a single domain in its equilibrium shape (Adamson & Gast 1997). In all thermodynamic hydration approaches just cited, global microstructure characteristics of the initial cement paste are accounted through the particle fineness and w/c, but only as input to the kinetic model of clinker phase dissolution (Parrott & Killoh 1984; Tomosawa 1997). Nevertheless, important properties of concrete, such as its elastic moduli and its permeability to liquids or gases depend on various details of the cement paste microstructure (Bentz 2000; Haecker et al. 2005; Promentilla et al. 2009; Schwartz et al. 1994). Therefore, attempts to predict the durability and service life of cement-based materials should be based on changes in cement paste microstructure.

In this report, we couple the thermodynamic approach to modeling cement hydration to a digital-image model of 3-D microstructure development. The combined thermodynamic/microstructural model, called THAMES, is applied to simulate the hydration of two OPCs, and the model predictions are compared to experimental measurements of the phase assemblage, porosity, compressive strength, and heat release. In addition, quantitative comparisons are made between the simulated microstructures and microstructures observed using scanning electron micrographs of polished sections of the hydrated cement pastes at different ages.

3.0 MATERIALS AND METHODS

Modeling results are compared to experimental measurements made on pastes of two different OPCs. Modeling the CBP cement will be addressed in Tasks 10 and 12 of the CBP project. The Cement and Concrete Reference Laboratory (CCRL) biannually issues pairs of proficiency samples of portland cement to be evaluated by hundreds of testing laboratories using ASTM standard test methods (ASTM 2000). The chemical characteristics and performance properties of these cements are, therefore, extremely well documented. Two of these cements were chosen for this report, hereafter designated as CCRL 151 (CCRL 2004a) and CCRL 168 (CCRL 2004b), in order to display and validate the current capabilities of THAMES.

3.1 Particle Size Distribution

The particle size distributions (PSDs) of both cements were determined using laser diffraction from a dilute suspension of particles in isopropyl alcohol. Six independent measurements were made for each cement, and the averages of these measurements are shown in Figure 2 as probability density functions. CCRL 168 is slightly finer than CCRL 151. The median effective diameter of CCRL 168 is 11 μm compared to 13 μm for CCRL 151. Blaine finenesses reported for CCRL 151 and CCRL 168 are 379 $m^2/kg \pm 13$ m^2/kg and 408 $m^2/kg \pm 10$ m^2/kg, respectively, as measured according to ASTM C204 (ASTM 2000) in the CCRL testing program (CCRL 2004a; CCRL 2004b).

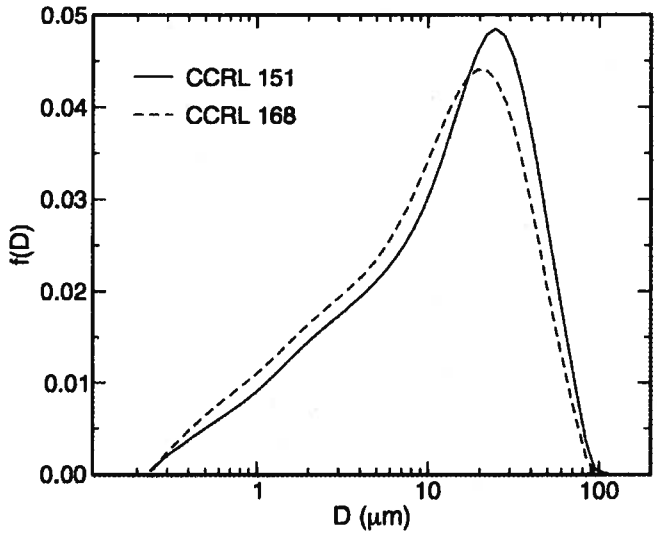

Figure 2. Particle size distributions, plotted as probability density functions, measured for cements CCRL 151 and CCRL 168 using laser diffraction from a dilute suspension of particles in isopropyl alcohol.

3.2 Cement Powder Image Processing and Phase Analysis

The preparation techniques for cement powder specimens analyzed by scanning electron microscopy (SEM) and X-ray microanalysis have been described in detail elsewhere (Stutzman 2007; Stutzman & Clifton 1999), so only a brief description will be given here. For analyzing the unhydrated cement powders, polished specimens were made by mixing the powder in an epoxy resin, curing the resin, and cutting to obtain a plane surface. Grinding and polishing were performed down to a 0.25-μm diamond paste, and the specimens were coated with carbon to provide a conductive surface.

Both backscattered electron (BE) and X-ray (XR) element images were collected simultaneously by SEM, using a typical accelerating voltage and current of 10 kV and 2 nA, respectively. XR maps were collected for Ca, Si, Al, Fe, S, K, Na, and Mg. Phase segmentation was based primarily on the BE images by correlating the local brightness levels to the phase average atomic number. The XR maps were used to facilitate distinction between phases with similar brightness levels, and to identify phases that are not easily detected in the BE images, such as periclase and alkali sulfates (Stutzman 2007).

Image segmentation was accomplished by multi-spectral processing as described in (Stutzman 2007). Noise reduction of the raw images was accomplished by median filtering and clipping, if necessary. The BE and XR images for a given image field are read into the hyperspectral data processing application Multispec©[2] (Landgrebe & Biehl 2001). Small portions of the image are used to establish training sets for phase identification, and a classifier, such as the Minimum Euclidean Distance or the Fischer Linear Likelihood classifiers (Landgrebe 2003) is employed to group like pixels. Example processed images of CCRL 151 and CCRL 168 are shown in Figure 3.

3.3 Stereological Analysis

Quantitative image analysis was performed on images of initial cement powders and of hydrated cement pastes for modeling and comparing microstructures. For the initial powders, segmented images like those in Figure 3 were analyzed quantitatively to determine properties of interest for creating representative starting 3-D microstructures for modeling. Properties of interest include the area fraction, surface perimeter fraction, and spatial distribution of each clinker phase was measured. Spatial distribution of phases was quantified by calculating various two-point correlation functions on the images, as described fully in (Bentz et al. 1999). Briefly, on an $M \times N$ digital image field, the two-point correlation function, $S_p(x,y)$, for a phase or collection of phases designated by p is given by

$$S_p(x,y) = \sum_{i=1}^{M-x} \sum_{j=1}^{N-y} \frac{I_p(i,j) \cdot I_p(i+x, y+j)}{(M-x)(N-y)} \quad \begin{matrix} 1 \le x \le M \\ 1 \le y \le N \end{matrix} \qquad (1)$$

where $I_p(x,y) = 1$ if the pixel at location (x,y) contains the phase or phases designated by p, and $I_p(x,y) = 0$ otherwise. Assuming that the microstructure is isotropic, $S_p(x,y)$ is transformed to a function of distance only, $S_p(r)$, where $r = \sqrt{x^2 + y^2}$. Correlation functions for isotropic materials are identical in 2-D and 3-D, so the correlation functions calculated on the final images like those in Figure 3 can be used directly to reconstruct 3-D microstructures with the same statistical spatial distribution of phases.

[2] Certain commercial materials and equipment are identified to adequately specify experimental procedures. In no case does such identification imply recommendation or endorsement by the National Institute of Standards and Technology, nor does it imply that the items identified are necessarily the best available for the purpose.

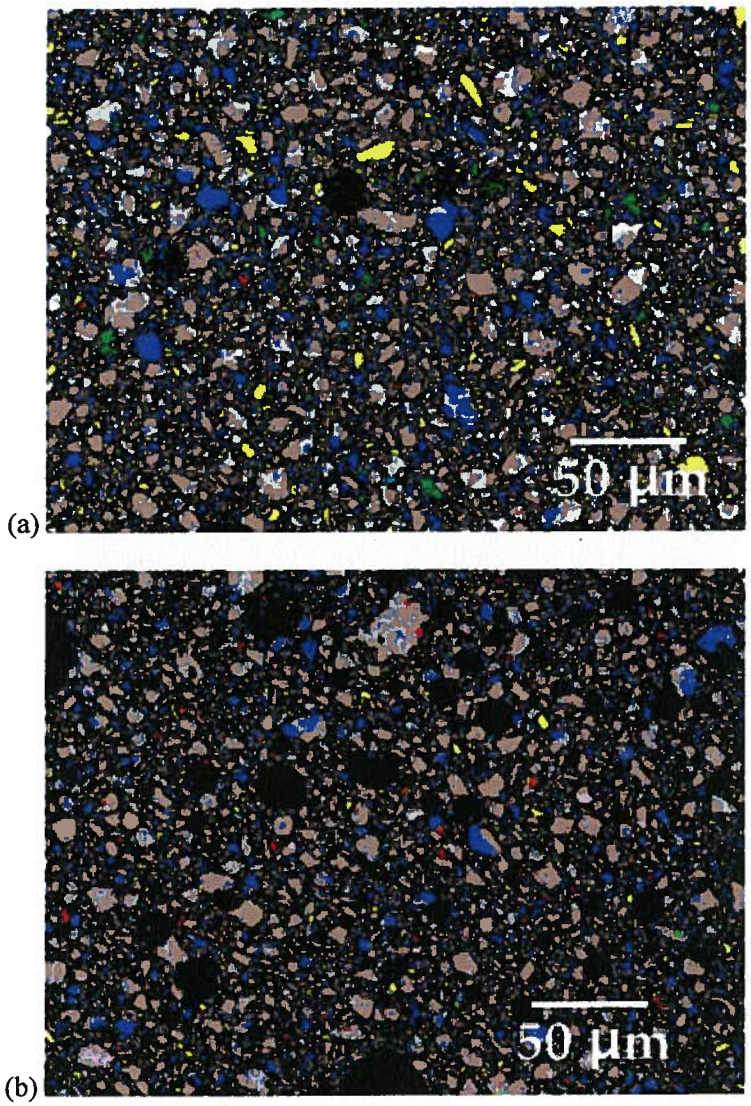

Figure 3. Final processed images of (a) CCRL 151 and (b) CCRL 168 with segmented phases identified by the following colors: C_3S (brown), C_2S (blue), C_3A (gray), C_4AF (white), gypsum/bassanite/anhydrite (yellow), calcite (green), periclase (pink).

Quantitative X-ray powder diffraction (QXRD) by Rietveld refinement was performed on both cement powders, using an internal standard of 11 % corundum (Al_2O_3) by mass. Table 1 gives the mass per cent of major oxide components in each cement, from which it can be seen that the major differences between the two cements is in the mass of MgO and K_2O, CCRL 168 being higher in both.

3.4 Tracking Hydration and Microstructure Development

Pastes of CCRL 151 and CCRL 168 were made by mixing the powder in 18-MΩ deionized water. For QXRD, 11 % corundum was added on a solids mass basis. The water-to-solids mass ratio was 0.45, which corresponds to a water-to-cement mass ratio w/c = 0.51.

Table 1. Major oxide components for CCRL 151 and CCRL 168 as measured by approximately 250 laboratories, reported as mass per cent. Values in parentheses represent one standard deviation in the reported measurements.

Oxide	CCRL 151 (%)	CCRL 168 (%)
CaO	64.73 (0.38)	62.28 (0.47)
SiO_2	20.03 (0.19)	19.91 (0.18)
Al_2O_3	4.91 (0.15)	5.11 (0.10)
Fe_2O_3	3.46 (0.07)	2.14 (0.05)
MgO	1.34 (0.07)	3.88 (0.11)
SO_3	3.12 (0.08)	3.48 (0.09)
K_2O	0.32 (0.02)	1.23 (0.03)
Na_2O	0.27 (0.03)	0.23 (0.04)

Table 2. Phase composition, in mass per cent of major phases in CCRL 151 and CCRL 168, based on Rietveld refinement of X-ray powder diffraction patterns using 11 % corundum by mass as an internal standard. Numbers in parentheses indicate within-laboratory 95 % confidence radius (Stutzman & Leigh 2007).

Phase/Mineral Name	CCRL 151 (%)	CCRL 168 (%)
C_3S	70.4 (2.04)	54.5 (2.04)
β-C_2S	9.2 (1.77)	15.7 (1.77)
C_3A (cubic)	4.4 (1.31)	8.0 (1.31)
C_4AF	11.4 (1.36)	7.0 (1.36)
Gypsum (dihydrate)	1.0 (0.59)	—
Bassanite (hemihydrate)	2.9 (1.08)	2.25 (1.08)
Anhydrite	0.36 (0.74)	0.19 (0.74)
Arcanite	0.65 (0.60)	1.07 (0.60)
Langbeinite	—	0.45 (0.60)
Aphthitalite	0.07	1.33 (0.60)
MgO (Periclase)	—	3.2 (0.63)
$CaCO_3$ (calcite)[b]	0.3 (2.73)	1.1 (2.73)
Present as solid solution in clinker phases[a]		
K_2O	0.00	0.0
Na_2O	0.18	0.11
MgO	1.4	0.7
SO_3	0.45	0.77

[a] Calculated based on thermogravimetric (TGA) measurements of the mass of CO_2.

[b] Based on total oxide measurements and mass fractions of K_2SO_4 and Na_2SO_4 determined by QXRD.

Characterization of the hydration products in cement paste by both SEM and QXRD presents a technical challenge. Both approaches have strengths and weaknesses, but the combination provides a detailed picture of the types and amounts of hydration products growing and the consumption of the residual cement phases. While QXRD analyses of cements are complicated, the analysis of hydration products introduces the additional complexity of an amorphous component from the water and initial poorly-ordered hydration products. Estimating the amorphous content requires the use of an internal standard, which was chosen to be corundum (NIST Standard Reference Material 676). Initial data and 24 h data were collected from a specimen holder that was sealed to retain moisture and exclude CO_2. At later ages, disks were cut from a cast cylinder of the paste using a low-speed diamond saw, and the cut disk surfaces were carefully lapped on a 1200-grit abrasive paper to minimize surface roughness. The Rietveld analysis utilizes calculated diffraction traces from crystal structure models. Most of these structures come from published data, while the hemicarboaluminate data were taken from Taylor (1997). The refinement proceeded in steps where diffraction patterns of selective extractions of the cements were refined and the structural and peak shape profile parameters were established. These parameters were subsequently fixed to avoid correlation problems in the more complex mixtures. The ordered C–S–H diffraction peak at 0.304 nm was fit using a calcite structure model where the peak shape was allowed to broaden to account for the diffraction peak intensity. Potential sources of bias in this approach stem

from the possibility of an incomplete accounting of all phases, possible errors associated with the hydration product models, and the use of the broadened calcite model to account for the diffraction peak of the ordered C–S–H. These potential sources of uncertainties will be further clarified in future Task 12 research.

SEM imaging uses backscattered electron and X-ray imaging to establish the spatial distribution of the constituent phases and is limited by the interaction volume, which is about 500 nm. This precludes discrete imaging of the fine needles of ettringite, but does provide insight into the phase identification of the more poorly-ordered constituents. For example, monosulfoaluminate is readily observed at later ages in cement pastes in the BE image where it exhibits a gray level similar to that of C–S–H, but with a more uniform texture and a platy parting. X-ray microanalysis of monosulfate also indicates the presence of aluminum, sulfur, and calcium. These characterization methods complement each other and the consensus estimates are most likely stronger estimates than either analysis individually.

3.5 Cement Particle Shape Characterization

Cement particle shape characterization has been carried out for CCRL Cement 151, and the same shapes were used for CCRL cement 168, as the main interest was comparing the effect of mineralogical differences between the two cements. The X-ray CT is used for 3-D particle shape characterization, along with spherical harmonic analysis (Erdogan et al. 2006; Garboczi 2002). Particles passing a #635 sieve (20 μm) are mixed in a dilute suspension in an epoxy, which is then hardened inside a 2 mm plastic cylindrical tube. Particles that pass through the #635 sieve that are about 4 μm to 20 μm are not considered, since the voxel size of the NIST X-ray CT scanner, about 1 μm to 2 μm per voxel, is not small enough to give at least 10 voxels across these particles, since this is what is needed to get accurate particle shape quantification (Taylor et al. 2006). The particles that are less than 1 μm to 2 μm will not be resolved at all and will only increase the background and make it harder to distinguish the shape of the larger particles. Recent work comparing sub-micrometer particles to particles that were 20 μm to 60 μm in diameter found that the shape differences were small, and did not really matter for hydration model performance (Holzer et al. 2010). So only characterizing the shape of the 20 μm to 60 μm diameter particles for use in THAMES at other particle sizes was considered to be adequate. For one given particle type (e.g., one cement, one sand), a database of about 2 000 to 100 000 particle shapes is measured and analyzed and can be drawn on when using GENMIC to prepare initial particle mixtures before hydration begins.

4.0 MODELING APPROACH

The modeling approach used in THAMES is a hybrid method by which thermodynamic calculations of bulk hydrated phase assemblage (GEMS), as a function of time, is coupled with a microstructure development model (EVOLVER) to estimate the spatial distribution of those phases.

4.1 Thermodynamic Calculations

The thermodynamic component of THAMES is identical to that described elsewhere by Lothenbach et al. (2008b). The change in mass of each of the four major clinker phases during a small time interval may be considered to disturb equilibrium between the pore solution and the hydrated phase assemblage by introducing Ca, Si, Al, Fe, and hydroxide into the pore solution. Equilibrium is considered to be re-established at the end of that time interval by changes in the mass of each hydrated phase. The mass change of the clinker phases during each time interval is estimated by the empirical model of Parrot and Killoh (1984). The compositions of the solid and liquid phases as a function of time and temperature are calculated based on

(i) the composition of the cement paste (Table 2),

(ii) the calculated degree of the dissolution of the clinker minerals (see description of kinetic model below), and

(iii) thermodynamic calculations using a self-consistent thermodynamic database

Thermodynamic modeling was performed using the Gibbs free energy minimization program GEMS (Kulik 2009). Chemical interactions involving solids, solid solutions, and aqueous electrolyte are considered simultaneously, including the speciation of dissolved species. The mass and, in the case of solid solutions, composition of each solid hydrate is computed as a function of time. The ultimate destination of dissolved alkali components is modeled using a distribution ratio R_d of 0.42 ml/g for uptake of both Na and K in C–S–H gel (Lothenbach & Winnefeld 2006). Thermodynamic data for aqueous species and some solids were taken from the PSI-GEMS thermodynamic database (Hummel et al. 2002), and solubility products for cement minerals were taken from compilations given in Lothenbach et al. (2008b) and Matschei et al. (2007). Minimization of the Gibbs free energy enables one to consider solid solution composition to be a function of liquid solution composition. The composition of C–S–H is assumed to follow the solid solution model originally developed by Kulik and Kersten (2001), while ideal solid solution substitution between Al and Fe is assumed for ettringite, monocarbonate, monosulfate, hemicarbonate, and hydrotalcite phases.

4.2 Reaction rates of Cement Clinker Phases

Dissolution of cement clinker provides the nutrients for formation of solid hydrates. The kinetic model of Parrot and Killoh (1984) describes the rate of dissolution of the four major clinker phases, C_3S, C_2S, C_3A, and C_4AF, by a set of empirical equations that attempt to describe the alternate rate-controlling mechanisms of hydration, including nucleation and growth of hydrated phases, diffusion of solute, etc. The rate of dissolution at any time by each of these mechanisms is assumed to depend on the instantaneous degree of hydration, w/c, and six empirical parameters for each phase. The empirical equations and values of the empirical parameters used in this study are given in (Lothenbach et al. 2008a) and will not be reproduced here.

4.3 Microstructure Modeling

Microstructure is modeled as a 3-D digital image, in which each voxel in a 100^3 array represents a volume of 1 μm^3 that is occupied by a single phase. The possible phases are each assigned positive integer identification numbers, hereafter called phase ids. The initial, unhydrated cement paste microstructure is created using GENMIC, which is similar to the Virtual Cement and Concrete Testing Laboratory software (Bullard & Stutzman 2006). First, digitized representations of cement particles are randomly parked in the digital image without overlap (Bentz 1997; Bentz 2005), each particle volume V_i being drawn from the measured PSD by assuming the PSD represents the distribution of "equivalent spherical diameters", i.e. the diameter of a sphere with volume V_i. Particles are placed in descending order of volume. The shape of each particle is created using a truncated spherical harmonic (SH) series. The SH coefficients of thousands of individual particles of CCRL 151 have been measured and stored for each particle in a database, and these particle database files are sampled at random from the database and given a 3-D orientation by assigning random values for the three Euler angles when creating the microstructure. The procedure is described in more detail in (Bullard & Garboczi 2006; Garboczi & Bullard 2004). Particle shapes for CCRL 151 were used for both cements in this study as the focus was on differences in chemistry, not particle shape. Reconstruction of the clinker phase volume fractions, surface area fractions, and spatial distribution in 3-D was performed after the generic particles were placed, using procedures and algorithms described elsewhere in detail (Bentz 1997; Bentz 2005).

Once the initial microstructure for a cement paste is created, the 3-D array is scanned once to identify the different interfaces between each of the solid phases and the solution. For each solid phase m, two lists are created. One of these is a "dissolution site" list $\{D\}_m$ which is the set all the voxels of phase m that are capable of dissolving because at least one nearest neighbor is occupied by solution. The other list is a "growth site" list $\{G\}_m$ which is the set of all solution voxels at which phase m can potentially grow because at least one nearest neighbor is also occupied by phase m.

After $\{D\}_m$ and $\{G\}_m$ are generated for each solid phase m, the members of the lists are evaluated for their potential to dissolve or grow, respectively. To evaluate these potentials, we assign "affinities" between solid phases, representing the relative tendency for the phases to grow in contact. A negative affinity between two solids means that they will tend to minimize their contact with each other, a positive affinity means they will tend to increase their contact with each other, and a zero affinity means that the phases will not be biased one way or the other. To encourage different kinds of growth morphologies, we enable a phase to have a positive, negative, or zero affinity for *itself*. For example, if a phase has a positive affinity for itself, growth of the phase will tend to occur at solution sites with greater numbers of itself as neighbors; a positive affinity will therefore tend to produce equiaxed and rounded shapes. On the other hand, if a phase has a negative affinity for itself, growth of the phase will tend to occur at solution sites with fewer numbers of itself as neighbors; this will tend to produce shapes with high aspect ratio and sharp corners. In the model, affinities are dimensionless integer values.

Table 3 gives the affinities used in these simulations. We emphasize that the concept of affinity as introduced here does not have any well-defined physical significance in terms of crystal growth theory, but instead is introduced as a mere convenience to generate different growth morphologies.

At the beginning of a simulation, the thermodynamic calculations are made as described in the previous section. The result of these calculations is a master table of the time dependence of the phase mass fractions, the first column storing the time in hours, and each of the other columns storing the volume fractions of a given phase. Thus the i-th row of the j-th column contains the volume fraction of phase j-1 in the microstructure at time t_i.

For the first time step, the first row of the master table is read. By comparing the target volume fractions in the table to the current volume fractions in the microstructure, a determination is made of the net number of voxels, N_m of each phase m that must be placed in the microstructure. The phase ids of a certain subset of the voxels in the microstructure are therefore changed to simulate microstructure development during that first time interval. To accomplish this, $\{D\}_m$ and $\{G\}_m$ are sorted in ascending and descending order, respectively, of their affinities for phase m. Then, for dissolution (or growth) of N_m voxels of phase m, the first N_m voxels in $\{D\}_m$ (or $\{G\}_m$) are switched to solution (or phase id m). We have observed that more realistic-looking microstructures are obtained if some randomness is imposed on the ordering of $\{G\}_m$. Therefore, we make random pair-wise swaps of the ordering of $\{G\}_m$ until a prescribed fraction of the growth sites, shown in Table 3 as the random growth/dissolution probability, have been affected. If a solid phase m must grow but $\{G\}_m$ is empty, then the phase is nucleated at randomly selected (x,y,z) locations where the nucleating phase is adjacent to a phase with which it has a high affinity in Table 3. Even if $\{G\}_m$ is not empty, a finite nucleation probability is defined for each growing phase, as shown in the last column in Table 3. The value of the nucleation probability is the probability that any given voxel of a phase that needs to grow will precipitate as a new embryo instead of attaching to existing surface of that phase. For these simulations, the nucleation probability of any particular phase is assumed to be a fixed value, although one expects it to be a function of the nucleation energy barrier and driving force for nucleation according to classical nucleation theory (Kashchiev & Rosmalen 2003). The values in Table 3 were chosen to make the spatial distribution of hydrated phases in the simulated microstructures similar to the experimentally observed ones, as described in the Results section.

Table 3. Interphase affinities, random growth probabilities, and nucleation probabilities assumed in the simulations. In column two, a number in parentheses next to a phase is the affinity for that phase. Only non-zero values are listed.

Phase	Affinities	Random Growth/Dissol. Probability	Nucleation Probability
C_3S	C_3S (1); $Ca(OH)_2$ (-1); C–S–H (4); Monocarbonate, AFm, Ettringite, C_3AH_6, Brucite, Hydrotalcite (-10)	0.001	0.0
C_2S	C_2S (1); $Ca(OH)_2$ (-1);	0.001	0.0
C_3A	C_3A (1)	0.001	0.0
C_4AF	C_4AF (1)	0.001	0.0
K_2SO_4	K_2SO_4 (1)	0.001	0.0
Na_2SO_4	Na_2SO_4 (1)	0.001	0.0
Gypsum	Gypsum (1)	0.001	0.01
Bassanite	Bassanite (1)	0.001	0.0
Anhydrite	Anhydrite (1)	0.001	0.0
$Ca(OH)_2$	C_3S, C_2S (-1)	0.8	0.1
C–S–H	C_3S, C_2S (4); Solution (2)	0.9	0.1
Monocarbonate	Monocarbonate, AFm, Ettringite (1); C_3S , C_2S (-10)	0.8	0.1
AFm	Monocarbonate, AFm, Ettringite (1); C_3S, C_2S (-10)	0.8	0.1
Ettringite	Ettringite (1); Solution (2); C_3S, C_2S (-10)	0.8	0.1
C_3AH_6	C_3AH_6 (1); Solution (2); C_3S, C_2S (-10)	0.8	0.1
Brucite	Brucite (1); Solution (2); C_3S, C_2S (-10),	0.8	0.1
Hydrotalcite	Hydrotalcite (1); Solution (2); C_3S, C_2S (-10)	0.8	0.1

Changing the phase ids of voxels in the microstructure will inevitably change the membership in the $\{D\}$ and $\{G\}$ lists. Sites formerly belonging to $\{G\}_m$ must be removed from $\{G\}_m$ if growth occurred there. Similarly, sites formerly belonging to $\{G\}_m$ must be removed from $\{G\}_m$ if they have been isolated from the solution by overgrowth of m or another solid phase. Therefore, after updating the phase ids of the affected voxels, $\{D\}$ and $\{G\}$ for each phase are updated and re-sorted. When updating $\{D\}$, any voxels containing a C–S–H phase are counted as also containing water in their gel porosity. Thus, for example, a C_3S voxel with C–S–H nearest neighbors is counted as a dissolution site for C_3S. Other than that, the criteria for membership in $\{D\}$ and $\{G\}$, and the sorting procedures, are the same as described previously.

5.0 RESULTS

5.1 Bulk Phases

Figure 4 compares, for the CCRL 151 paste (w/c = 0.45), the measured and predicted time dependences of the masses of the four major clinker phases and of four of the major hydrated phases, C–S–H gel, CH, ettringite, and monosulfate, for sealed curing conditions at 23 °C. The masses all reported as mass fractions, normalized to the total system mass (solid plus solution). With the exception of C_4AF, the kinetic model gives reasonably good fits to the consumption of the clinker phases. In addition, the model somewhat overestimates the mass fraction of CH and ettringite, and significantly overestimates the mass fraction of monosulfate after 72 h.

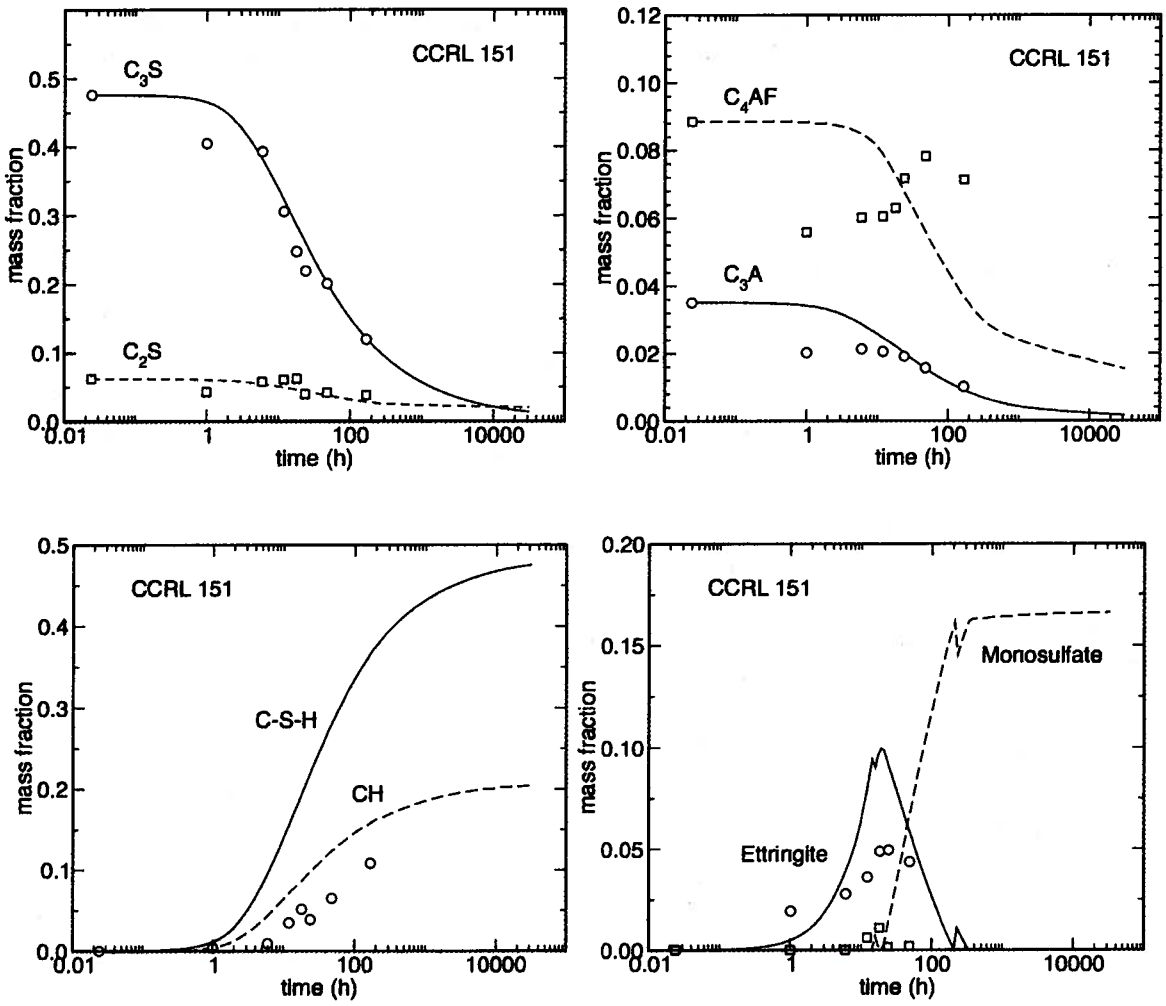

Figure 4. Mass fractions of the four major clinker phases, C–S–H gel, CH, ettringite, and monosulfate as a function of time in CCRL 151 paste (w/c = 0.45) hydrated at 23 °C under sealed conditions. Continuous and dashed curves are model predictions. Open symbols are experimental measurements made by QXRD. QXRD measurements of C–S–H gel are not available. Uncertainties in the experimental data, estimated as one standard deviation of ten analyses, are: CH = 0.02 to 0.03, AFt = 0.02 to 0.06, C_3S = 0.01 to 0.03, C_2S = 0.006 to 0.02, C_3A = 0.01, C_4AF = 0.015.

Figure 5 shows the same phase information as Figure 4 but for CCRL 168. Again, the kinetic model provides reasonable fits to the consumption of the four major clinker phases, although in general it appears to somewhat overestimate the amount of each phase remaining at any given time. The model predicts the mass fraction of CH better for CCRL 168 than it does for CCRL 151. The greatest discrepancies occur for ettringite and monosulfate. If one accounts for the 1.1 % calcite present in the cement (see Table 2), the ettringite phase remains remarkably stable at later ages because of the presence of the monocarbonate phase which forms preferentially to monosulfate. This is represented by the dashed lines in Figure 5 for ettringite and monosulfate. However, although the experimental data indicate very little monosulfate forming at later ages, those data also indicate that some monosulfate forms at earlier times before the sulfate sources are consumed at about 90 h. Reductions in both the monosulfate and ettringite mass fractions is observed after about 90 h, but the dashed line for ettringite indicates that very little reduction is expected.

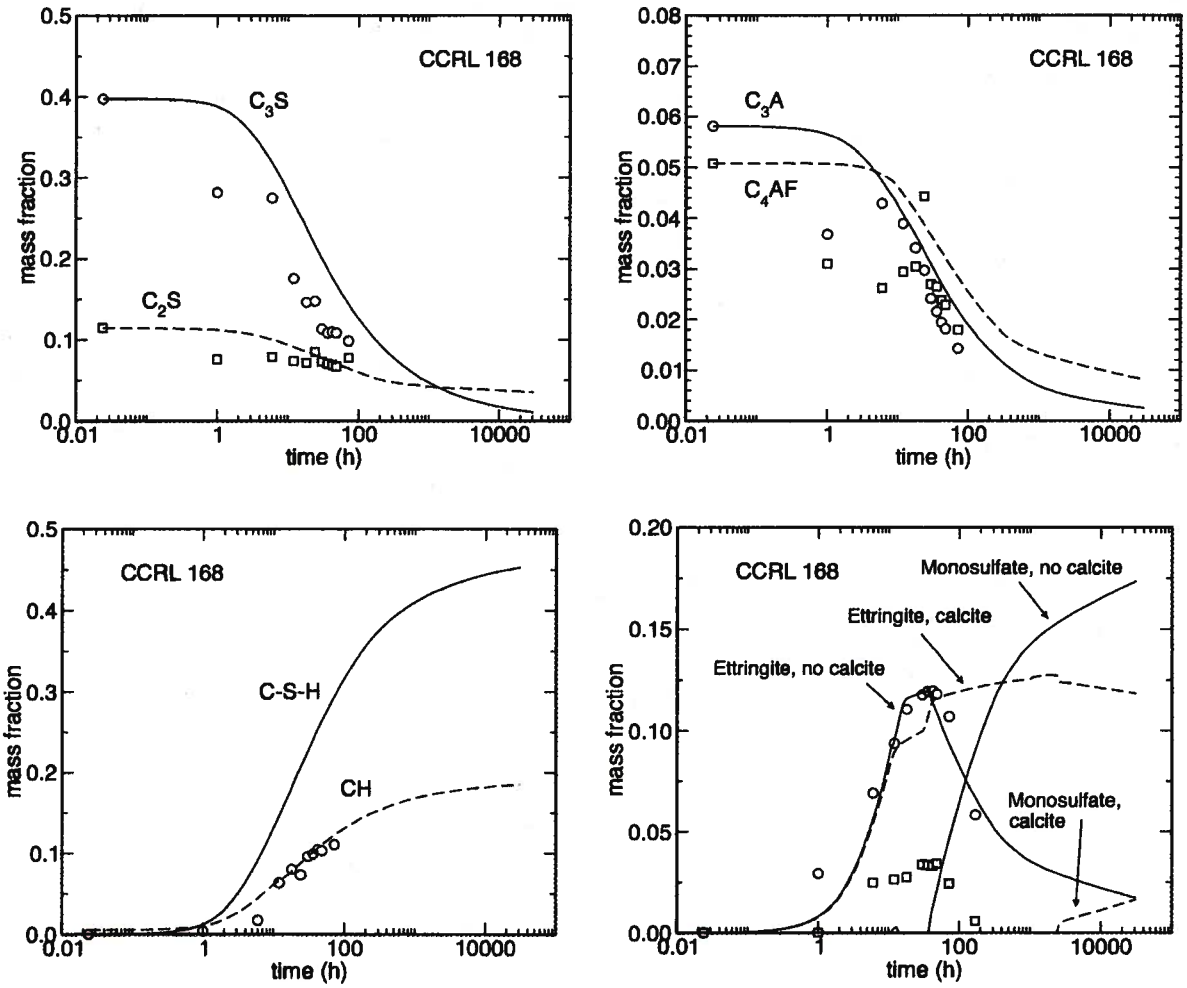

Figure 5. Mass fractions of the four major clinker phases, C–S–H gel, CH, ettringite, and monosulfate as a function of time in CCRL 168 paste (w/c = 0.45) hydrated at 23 °C under sealed conditions. Continuous and dashed curves are model predictions. Open symbols are experimental measurements made by QXRD. QXRD measurements of C–S–H are not available. The solid and dashed lines for ettringite and monosulfate correspond to calculations with calcite excluded and included in the cement, respectively. Uncertainties in the experimental data are the same as in Figure 4.

The calcite mass fractions reported in Table 2 are inferred from TGA measurements. If any free lime in the cement reacts with residual carbon dioxide in the atmosphere during heating of the powder sample, then the calcite mass fraction will be overestimated. Data for CCRL 151 indicates that this conversion happens readily during heating in air (Bullard & Stutzman 2006), so it is legitimate to question the initial calcite content in CCRL 168. Therefore, we also conducted simulations on CCRL 168 in which the inferred calcite content in the cement was neglected. In these simulations (the solid lines for ettringite and monosulfate in Figure 5) the fit of the model to the experimental data is much better for ettringite. In addition, the monosulfate phase is predicted to form earlier, which is also more consistent with the experimental data than when calcite is not neglected. This time, however, the model significantly overestimates the amount of monosulfate at later ages. The better agreement to the ettringite data in the absence of calcite in Figure 5 suggests that the calcite content has been overestimated. When calcite in the initial powder is neglected, the model significantly overestimates the amount of monosulfate at later ages. At this point, we cannot readily account for the early formation of monosulfate, between 8 h and 36 h, nor for its apparent disappearance at later ages.

5.2 Heat of Hydration and Compressive Strength

The heats of hydration at 7 d and 28 d were measured for both cements by the testing laboratories, using the ASTM C186 heat of solution test method (ASTM 2000). Figure 6 shows the mean values with the error bars representing plus/minus one standard deviation. The model tracks the isothermal heat release from the paste continuously because it accounts for the enthalpy of formation of each solid phase and solute species. The continuous curves show the model predictions using a cement paste with w/c = 0.4 cured isothermally at 23 °C under sealed conditions. The fit to the experimental data is quite good for CCRL 168, but the model overestimates the heat release at both times for CCRL 151. This is not too surprising in light of the fact that the model overestimates the mass fractions of CH and ettringite as CCRL 151 hydrates (see Figure 4).

For simulating the compressive strengths of mortar cubes, as measured by the ASTM C109 test method (ASTM 2000), simulations were run for pastes of both CCRL 151 and CCRL 168 at w/c = 0.485, using isothermal curing at 23 °C under sealed conditions. From each simulation, we calculate the Powers gel-space ratio, X, defined as the ratio of the combined volume of all hydration products (the gel), to the sum of the gel volume and the volume of capillary pores. The mortar cube compressive strength, σ, is estimated from X as a function of time, t, according to the following relation recommended by Taylor (1997):

$$\sigma(t) = AX(t)^n \qquad (2)$$

For each cement paste, the values of A and n in Eq. 2) were determined by fitting to the experimental data at 3 d and 7 d. Figure 7 shows the simulation results and the experimental data measured by the testing laboratories at 3 d, 7 d, and 28 d. Because of the fitting procedure, the only meaningful comparison can be made at 28 d. The calibrated Eq. (2) fits the 28 d strength well within the experimental uncertainty. Further testing is required on a wider range of cement pastes, but it may be possible to make reasonable strength predictions with the model by fitting only the lead coefficient A using the measured strength at 3 and fixing the exponent at a value of 1.8.

The linear elastic moduli and ionic diffusivity may also be computed at the cement paste length scale using finite element techniques for the elastic moduli (Haecker et al. 2005) and finite difference techniques (Garboczi & Bentz 1992). Both of these techniques have been well-validated against experimental data. Results will be generated in the FY2010 Task 10 work.

The fluid permeability may also be estimated (Garboczi & Bentz 2001; Garboczi, Bentz & Martys 1999), but since this property is very sensitive to pore size, a much larger THAMES model must be made in order to have the resolution needed for realistic size pores (i.e. 0.1 μm). This will involve parallelization of THAMES, which will be considered in the later stages of Task 10.

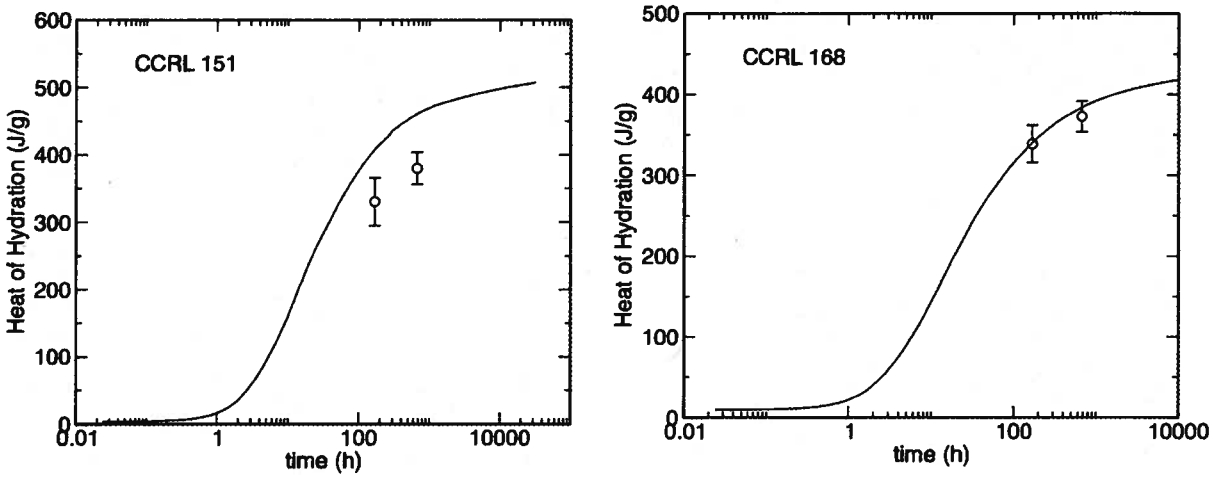

Figure 6. Predicted time dependence of the heat release in CCRL 151 and CCRL 168 pastes (w/c = 0.40) cured under sealed conditions at 23 °C. Continuous curves are model predictions. Open circles are the mean values measured at 168 h (7 d) and 672 h (28 d), and the error bars represent plus/minus one standard deviation of approximately 20 measurements each (CCRL 2004a; CCRL 2004b).

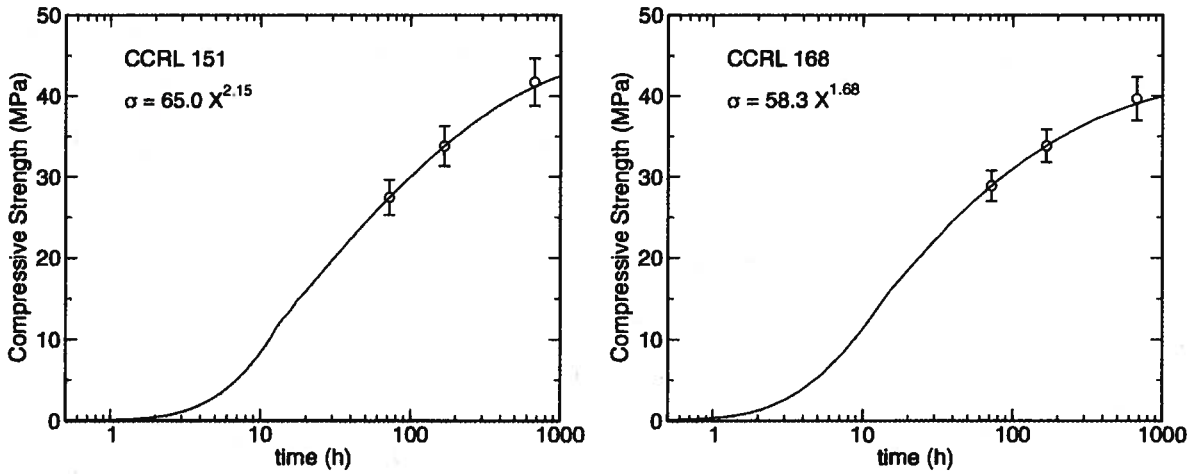

Figure 7. Predicted time dependence of the compressive strength in CCRL 151 and CCRL 168 mortars (w/c = 0.485) cured under sealed conditions at 23 °C. Continuous curves are model predictions using the gel-space ratio equation given in each plot. Open circles are the mean values measured at 72 h (3 d),168 h (7 d) and 672 h (28 d), and the error bars represent plus/minus one standard deviation of approximately 200 measurements each (CCRL 2004a; CCRL 2004b).

5.3 Microstructure Development

All the simulation results in the previous section involved only bulk phase quantities as a function of time. In this section, we compare the spatial distribution of the phases in the microstructure of CCRL 168 to experimental observations. This is an important comparison, since THAMES is a 3-D **microstructure** model, not just a cement hydration model.

Figure 8 shows SEM images of polished sections of CCRL 168 paste hydrated for 7 d at 23 °C under sealed conditions, and Figure 9 shows two representative slices from the simulated 3-D microstructure at the same time. The two figures are at different magnifications; the white dashed box in Figure 8 indicates the areas shown in Figure 9. The simulated microstructures appear to compare favorably to the observed microstructure. For example, both microstructures show an intimate intermixing of hydration products in the outer product, the unhydrated particle morphologies are similar, and the location and spacing of the larger capillary pores are similar.

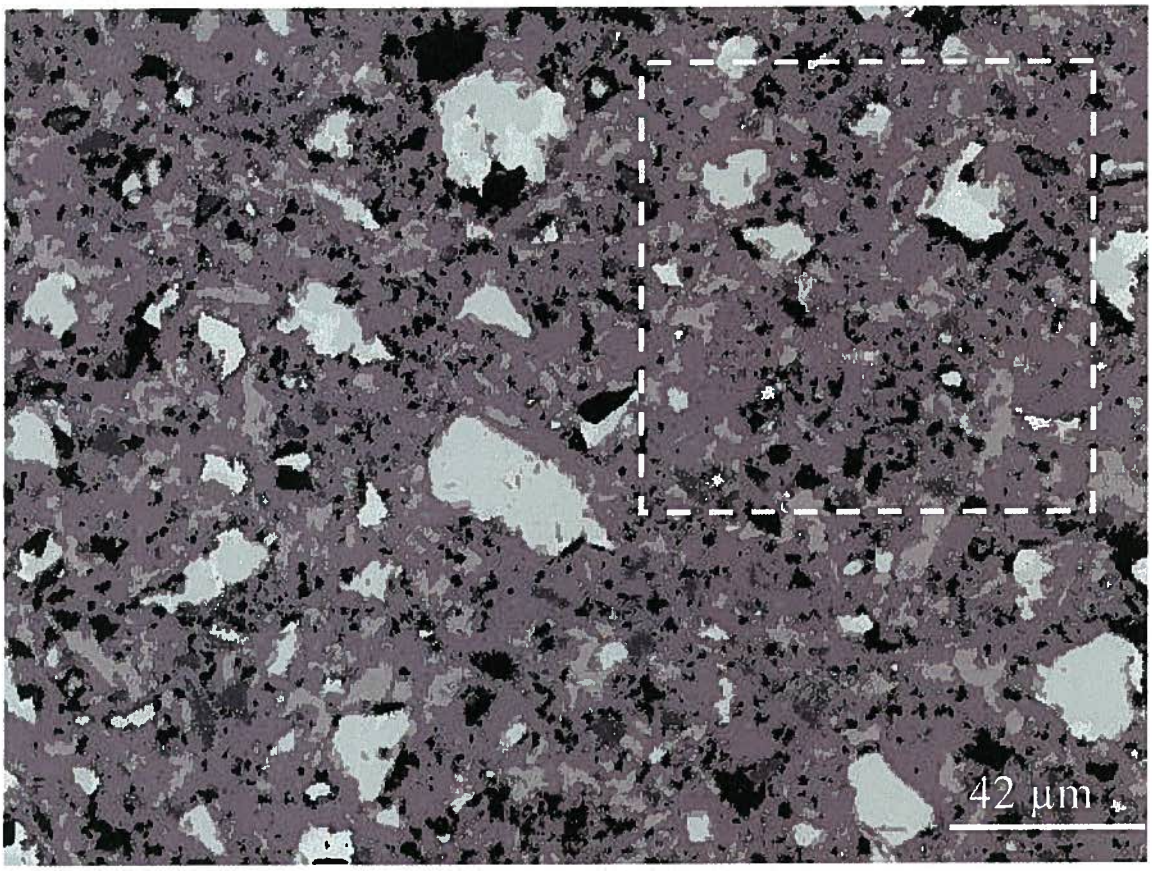

Figure 8. SEM images of polished sections of CCRL 168 paste hydrated for 7 d at 23 °C under sealed conditions. The images have been segmented into the following phase collections, in order of decreasing brightness in the images: clinker silicates, clinker interstitial phases, CH, C–S–H gel, monosulfate, ettringite, and capillary pores. The dashed box shows the relative volume of the simulated system in Figure 9.

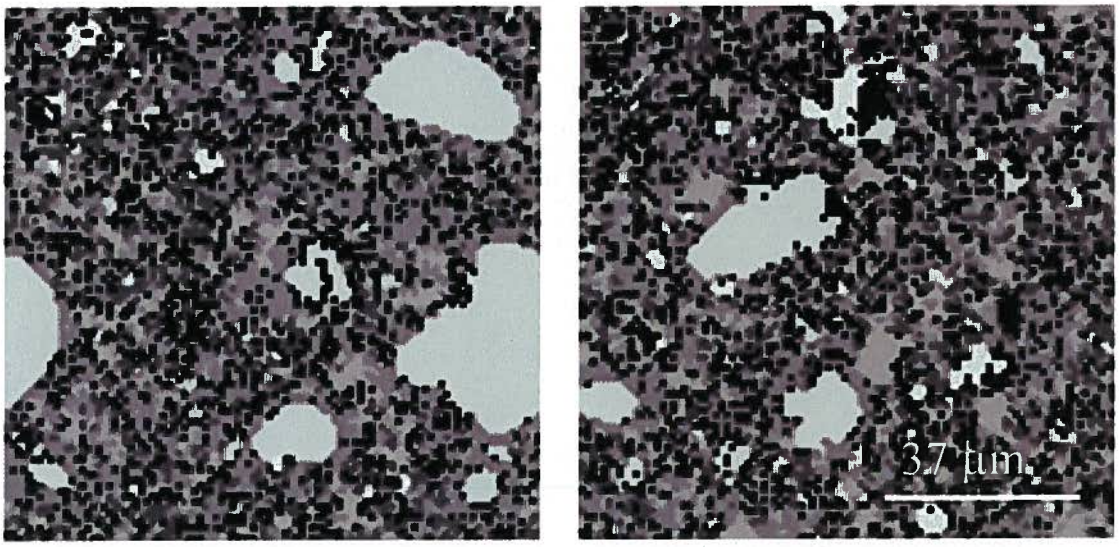

Figure 9. Slices of the simulated microstructure of CCRL 168 paste hydrated for 7 d at 23 °C under sealed conditions. The brightness of the phases follows the same ranking as in the SEM images in Figure 8.

Quantitatively, the simulated and observed microstructures have similar volume fractions of the major unhydrated and hydrated solid phases, with the exception of ettringite, as already shown in Figure 5. In addition, we can make a semi-quantitative comparison of the spatial distribution of the major phases by using two-point correlation functions. Figure 10 shows the observed and simulated correlation functions for the microstructures in Figure 8 and Figure 9, respectively. In both figures, the plots have been normalized to the value of the correlation function at r = 0, to reduce the effect of the differences in volume fractions of the phases in the real and simulated microstructures. The agreement between the real and simulated microstructures is reasonably good, especially for CH and the unhydrated cement. The differences at larger distances for the capillary porosity are due primarily to the differences in calculated total porosity and that observed in the micrograph in Figure 8. Although each curve has been normalized to its value at r = 0, which is the volume fraction ϕ of the phase(s) in the corresponding microstructure, the limiting value of the correlation function at larger distances is ϕ^2 in a perfectly random microstructure. Normalizing the curves by ϕ therefore reduces, but does not eliminate, the systematic differences at large distances.

The differences between real and simulated correlation functions for combined ettringite plus monosulfate at large distances in Figure 10 is, again, due to the difference in volume fraction of the combined phases. The volume fraction of ettringite plus monosulfate in the simulated microstructures was 0.16, but in the piece of microstructure shown in Figure 8, it is only 0.04. This value is much lower than the volume fraction found by using the X-ray diffraction data, about 0.1 at 7 d (see Figure 5).

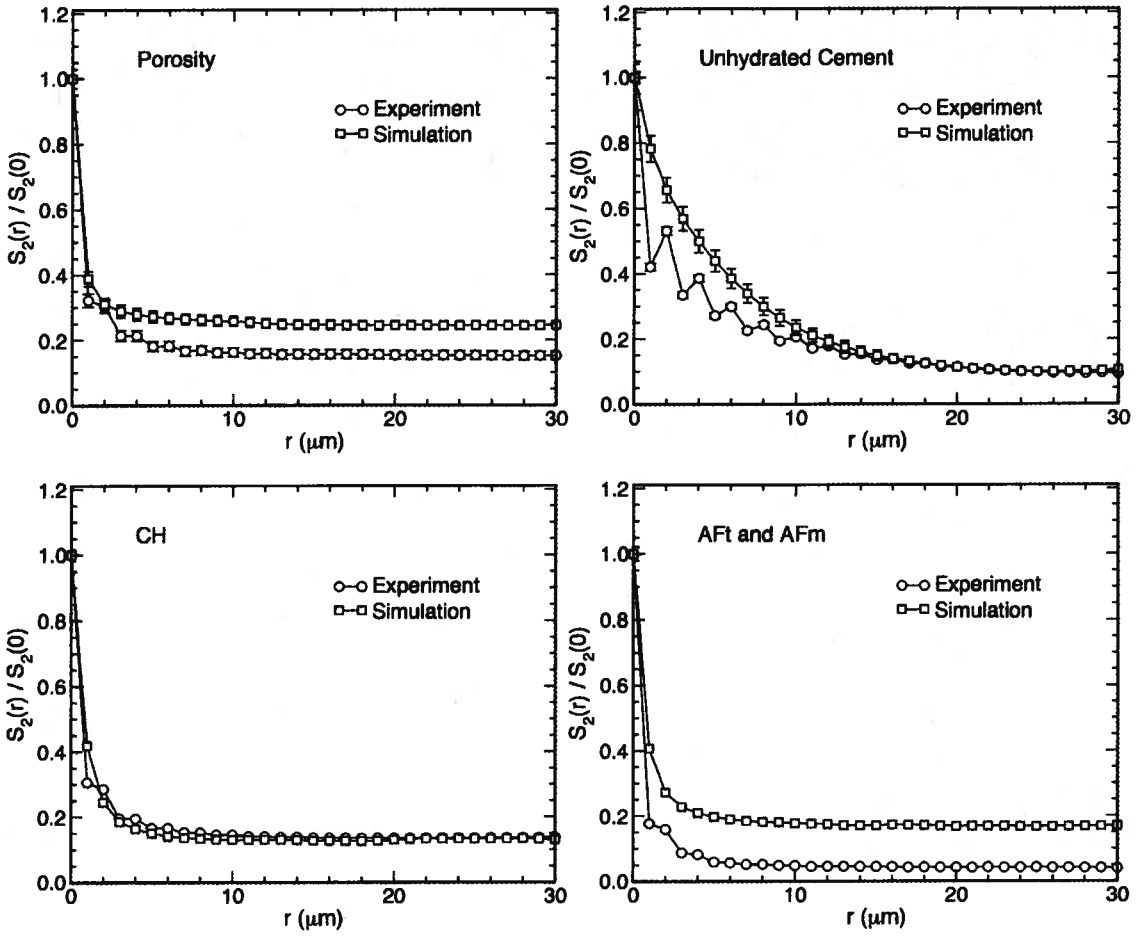

Figure 10. Two-point correlation functions as a function of distance, r, normalized by their values at r = 0, for the simulated hydration of CCRL 168 with w/c = 0.45, including capillary porosity, unhydrated cement grains, CH, and combined ettringite (AFt) and monosulfate (AFm) phases. Error bars for the simulations represent plus/minus one standard deviation at each point for five different 2-D slices of the microstructure.

6.0 MAKING PREDICTIONS AT THE MORTAR AND CONCRETE LENGTH SCALES (CONCPROPS)

The module CONCPROPS will take the cement paste-level predictions made by THAMES and use them to make mortar and concrete-level predictions. The properties of the aggregates (sand and gravel) need also to be known in order for CONCPROPS to give accurate predictions. These include the aggregate size and shape distributions, their physical properties like elastic moduli, and, for long-term durability modeling, their mineralogical composition including susceptibility to things like alkali-silica attack.

A combination of paste-scale simulations and effective medium theory is used to make mortar and concrete-scale predictions. The paste-scale simulations are used to investigate how the porosity scales with distance from the paste-aggregate interface (Sun, Garboczi & Shah 2007). This information is then incorporated into three-phase effective medium theory for either diffusive (Garboczi & Berryman 2000) or elastic properties (Garboczi & Berryman 2001) of the mortar or concrete, using the aggregate size and shape distribution.

These models have been incorporated into the latest version of the Virtual Cement and Concrete Testing Laboratory (VCCTL). CONCPROPS will involve a simpler way of linking these models to the main THAMES models and will be developed in Task 10, starting in FY2011, so that these models can be easily coupled to the THAMES paste-level output in the eventual integrated CBP model.

Aggregate size characterization is done using laser diffraction techniques, for finer sand, and sieve analysis, for larger particles. Since laser diffraction can distort the true size distribution for non-spherical particles (Bowen, Sheng & Jongen 2002; Erdogan, Garboczi & Fowler 2007; Gabas, Hiquily & Laguérie 1994), X-ray CT is also carried out for these particles in a manner similar to that for the cement particles (Erdogan et al. 2006; Garboczi 2002). This shape characterization for the CBP materials (cement, fly ash, slag, sand, gravel) will be carried out in Task 12. The details of the relevant procedures will be given in Task 12 reports.

7.0 DISCUSSION

Modeling of cement hydration and microstructure development can be used as a research tool to understand hydration mechanisms and the effects of chemical admixtures on hydration rates, and to explore the nature of material incompatibilities in cement blends. It can also be used to reconstruct realistic microstructures that can subsequently be employed to calculate or estimate material properties that influence performance and service life, which is main purpose of THAMES as it is planned to be used in the eventual integrated CBP model.

Several recent publications have demonstrated that bulk properties, i.e. those that depend only on the total amounts of each phase, can be reasonably estimated for a variety of cement types using only equilibrium thermodynamic calculations coupled with empirical kinetic equations for the dissolution rate of clinker phases (Guillon, Chen & Chanvillard 2008; Lothenbach et al. 2008a; Lothenbach & Wieland 2006; Lothenbach & Winnefeld 2006). But properties that depend on microstructure are more difficult to estimate because the emergent microstructure is sensitive to the kinetic rate laws and anisotropy of growth and dissolution by which it is governed. Our approach here has been to estimate microstructural changes by using a few simple rules for growth and dissolution, tailored to each phase, as summarized in Table 3. As already described, the rules we have used for simulating growth and dissolution were not derived from any fundamental physical or chemical principles. Instead, the rules were developed to simulate nucleation and coherent growth or dissolution at interfaces with some built in randomness that can be tuned for each phase. The rule parameters were chosen to produce simulated microstructures that compare favorably to experimentally observed microstructures both in their qualitative appearance and in their two-point correlation functions.

Microstructure-dependent properties such as the effective elastic and viscoelastic moduli, gas and liquid permeabilities, and diffusion formation factor all can be calculated using finite difference or finite element methods on a 3-D digitized microstructure image (Bentz et al. 2000). Some of these properties, particularly the elastic moduli, depend primarily on the volume fraction of each solid phase and the connectivity of the solid structure. The dependence of these properties on finer details of the microstructure is fairly weak. But other properties, such as permeability, depend much more strongly on the distribution in size and shape of pores across multiple length scales. A simulated microstructure must have greater fidelity to the actual microstructure to make accurate calculations of these latter properties. Good matches to the two-point correlation functions will not guarantee that the microstructure is accurate enough. A more satisfactory test of the microstructure would compare the actual pore size distribution, measured by gas adsorption or low-temperature calorimetry, to the pore size distribution measured on the actual microstructure. Large, parallel versions of THAMES will be required for the task of computing permeability, since the length per voxel will need to be lowered in order to represent the smaller pores correctly. Finite difference models for computing fluid flow in porous materials have already been developed (Garboczi, Bentz & Martys 1999).

The pore space in cement paste is extremely complex topologically, and has important features on length scales ranging from nanometers to micrometers. The simulations presented in this paper have a lattice spacing of 1 μm; neither capillary pores smaller than 1 μm, nor the gel porosity, can be resolved in these simulations,

so we would not expect to be able to make accurate calculations of transport properties. To include such small pores explicitly, one would need to run the simulations at a lattice resolution of a few nanometers. But this strategy is not currently feasible for at least two reasons. First, it would require about 10^{12} lattice sites to include a representative volume element of cement paste, about 10^6 μm^3, while still resolving the smallest pores. This number of lattice sites is too large, by several orders of magnitude, to be simulated with this model or with any of the finite difference or finite element models for calculating transport properties. In addition, even if these computational limitations could be overcome, the physics of C–S–H growth at these length scales is not well understood, so formulating nanoscale C–S–H growth rules that would accurately reproduce the gel pore morphology for the different types of C–S–H (Allen, Thomas & Jennings 2007; Richardson 2004) would be a major challenge. A more effective strategy for including small pores probably would employ a constitutive model of the pore volume and morphology in the different forms of C–S–H as a function of their growth conditions and age. Such a constitutive model would need to draw heavily on experimental measurements of C–S–H gel pore structure by gas adsorption (Jennings 2000) , by neutron scattering techniques (Allen, Thomas & Jennings 2007), and by direct microscopic examination (Richardson 2004). For computing permeability, a Brinkman's equation approach would work. This approach combines Navier-Stokes fluid flow in the capillary pores (which are imaged as pores) and Darcy's law permeability in the C–S–H phase (which is only resolved as a continuum material) (Martys, Bentz & Garboczi 1994; Martys 2001; Martys & Hagedorn 2002).

8.0 SUMMARY AND PROSPECTUS

A numerical model, THAMES, has been described for simulating the microstructure development of hydrating cement paste. The model couples three separate "sub-models": an empirical model of the dissolution kinetics of the four major clinker phases, an equilibrium thermodynamic model for determining the phase assemblage based on equilibrium with the pore solution, and a rule-based digital image model for incrementally changing the 3-D microstructure in a way that is consistent with the thermodynamic calculations. This model has been tested here on two ordinary portland cement pastes, and reasonable agreement between simulation and experiment was obtained for the bulk phase volume fractions at any time beyond about 10 hours of hydration. In addition, the actual and simulated microstructures were mostly in good qualitative and quantitative agreement, both in terms of the microstructure appearance and the two-point correlation functions. THAMES also provides good agreement with the measured 28-d compressive strength of ASTM C109 mortar cubes and the heat of hydration.

A major challenge for this kind of model is to improve its applicability for producing microstructures that can be used to accurately calculate fluid transport properties. This requires further research to develop constitutive models for C–S–H gel pore size and shape distributions as a function of growth conditions. A second challenge is to extend the model to simulate hydration of cements containing supplementary cementitious materials (SCMs). The thermodynamic model has been successfully used to simulate the influence of limestone additions to portland cement, but the microstructure development model has not yet been tested on such systems. Even more importantly, for SCMs such as blast-furnace slag and fly ash, general kinetic models for their dissolution rates as a function of composition and fineness do not yet exist. Developing models for slag and fly ash dissolution rates is a major challenge that must be addressed before the thermodynamic model or the microstructure model can be applied to such systems. Finally, limited experimental observations have indicated that the nanostructural properties of C–S–H gel change slowly with age and also depend significantly on the composition of the cement (Richardson 2004). Again, constitutive models will be required to account for these changes in C–S–H, especially when simulating microstructures that are decades or centuries old.

9.0 REFERENCES

Adamson, AW & Gast, AP 1997, *Physical Chemistry of Surfaces, 6th Edition*, John Wiley & Sons, New York, NY.

Allen, AJ, Thomas, JJ & Jennings, HM 2007, 'Composition and density of nanoscale calcium-silicate-hydrate in cement', *Nature Materials* vol. 6, no. 4, pp. 311-316.

ASTM 2000, *Annual Book of ASTM Standards, vol. 04.01*, American Society for Testing and Materials, West Conshohocken, PA.

Bentz, DP 1997, 'Three-dimensional computer simulation of cement hydration and microstructure development', *Journal of the American Ceramic Society*, vol. 80, no. 1, pp. 3-21.

Bentz, DP 2000, 'Influence of silica fume on diffusivity in cement-based materials: II. Multi-scale modeling of concrete diffusivity', *Cement and Concrete Research*, vol. 30, no. 7, pp. 1121-1129.

Bentz, DP 2005, *CEMHYD3D: A three-dimensional cement hydration and microstructure development modeling package. Version 3.0*, NISTIR 7232, U.S. Department of Commerce. Available from: http://concrete.nist.gov/monograph.

Bentz, DP, Jensen, OM, Coats, AM & Glasser, FP 2000, 'Influence of silica fume on diffusivity in cement-based materials: I. Experimental and computer modeling studies on cement pastes', *Cement and Concrete Research*, vol. 30, no. 6, pp. 953-962.

Bentz, DP, Stutzman, PE, Haecker, C-J & Remond, S 1999, 'SEM/X-ray imaging of cement-based materials', in *Proceedings of the 7th Euroseminar on Microscopy Applied to Building Materials*, eds HS Pietersen, JA Larbia & HHA Janssen, Delft University of Technology, pp. 457-466.

Bowen, P, Sheng, J & Jongen, N 2002, 'Particle size distribution measurement of anisotropic--particles cylinders and platelets--practical examples', *Powder Technology*, vol. 128, no. 2-3, pp. 256-261.

Bullard, JW & Garboczi, EJ 2006, 'A model investigation of the influence of particle shape on portland cement hydration', *Cement and Concrete Research*, vol. 36, no. 6, pp. 1007-1015.

Bullard, JW & Stutzman, PE 2006, 'Analysis of CCRL proficiency cements 151 and 152 using the Virtual Cement and Concrete Testing Laboratory', *Cement and Concrete Research*, vol. 36, no. 8, pp. 1548-1555.

CCRL 2004a, *Final Report: Portland Cement Proficiency Samples Number 151 and Number 152*, National Institute of Standards and Technology Gaithersburg, Maryland. Available from: http://www.ccrl.us/.

CCRL 2004b, *Final Report: Portland Cement Proficiency Samples Number 167 and Number 168*, National Institute of Standards and Technology Gaithersburg, Maryland. Available from: http://www.ccrl.us/.

Erdogan, ST, Garboczi, EJ & Fowler, DW 2007, 'Shape and size of microfine aggregates: X-ray microcomputed tomography vs. laser diffraction', *Powder Technology*, vol. 177, no. 2, pp. 53-63.

Erdogan, ST, Quiroga, PN, Fowler, DW, Saleh, HA, Livingston, RA, Garboczi, EJ, Ketcham, PM, Hagedorn, JG & Satterfield, SG 2006, 'Three-dimensional shape analysis of coarse aggregates: New techniques for and preliminary results on several different coarse aggregates and reference rocks', *Cement and Concrete Research*, vol. 36, no. 9, pp. 1619-1627.

Gabas, N, Hiquily, N & Laguérie, C 1994, 'Response of Laser Diffraction Particle Sizer to Anisometric Particles', *Particle and Particle Systems Characterization*, vol. 11, no. 2, pp. 121-126.

Garboczi, EJ 2002, 'Three-dimensional mathematical analysis of particle shape using X-ray tomography and spherical harmonics: Application to aggregates used in concrete', *Cement and Concrete Research*, vol. 32, pp. 1621-1638.

Garboczi, EJ & Bentz, DP 1992, 'Computer simulation of the diffusivity of cement-based materials', *Journal of Materials Science*, vol. 27, no. 8, pp. 2083-2092.

Garboczi, EJ & Bentz, DP 2001, 'The effect of statistical fluctuation, finite size error, and digital resolution on the phase percolation and transport properties of the NIST cement hydration model', *Cement and Concrete Research*, vol. 31, pp. 1501-1514.

Garboczi, EJ, Bentz, DP & Martys, NS 1999, 'Digital images and computer modelling', in *Experimental Methods for Porous Media*, ed. P-z Wong, Academic Press, New York, NY.

Garboczi, EJ & Berryman, J-G 2000, 'New effective medium theory for the diffusivity or conductivity of a multi-scale concrete microstructure model', *Concrete Science and Engineering*, vol. 2, no. 6, pp. 88 - 96.

Garboczi, EJ & Berryman, JG 2001, 'Elastic moduli of a material containing composite inclusions: effective medium theory and finite element computations', *Mechanics of Materials*, vol. 33, no. 8, pp. 455-470.

Garboczi, EJ & Bullard, JW 2004, 'Shape analysis of a reference cement', *Cement and Concrete Research*, vol. 34, no. 10, pp. 1933-1937.

Guillon, E 2004, 'Durabilité des matériaux cimentaires: modélisation de l'influence des équilibres physico-chimiques sur la microstructure et les propriétés mécaniques résiduelles', Ph.D. thesis, Cachan, France.

Guillon, E, Chen, J & Chanvillard, G 2008, 'Physical & chemical modelling of the hydration kinetics of OPC paste using a semi-analytical approach', *Proceedings of the CONMOD'08 International RILEM Symposium on Concrete Modelling*, Delft University of Technology.

Haecker, C-J, Garboczi, EJ, Bullard, JW, Bohn, RB, Sun, Z, Shah, SP & Voigt, T 2005, 'Modeling the linear elastic properties of Portland cement paste', *Cement and Concrete Research*, vol. 35, no. 10, pp. 1948-1960.

Holzer, L, Flatt, RJ, Erdoğan, ST, Bullard, JW & Garboczi, EJ 2010, 'Shape comparison between 0.4 mm to 2.0 mm and 20 mm to 60 mm cement particles', *Journal of the American Ceramic Society*, vol. (in press).

Hummel, W, Berner, U, Curti, E, Pearson, FJ & Thoenen, T 2002, *Nagra/PSI chemical thermodynamic data base 01/01*, Nagra Technical Report NTB 02-16, Wettingen, Switzerland.

Jennings, HM 2000, 'A model for the microstructure of calcium silicate hydrate in cement paste', *Cement and Concrete Research*, vol. 30, no. 1, pp. 101-116 and references therein.

Kashchiev, D & Rosmalen, GMv 2003, 'Review: Nucleation in solutions revisited', *Crystal Research and Technology*, vol. 38, no. 7-8, pp. 555-574.

Kulik, D, *GEMS-PSI 2.03*, PSI, Villigen, Switzerland. Available from: http://gems.web.psi.ch/.

Kulik, DA & Kersten, M 2001, 'Aqueous Solubility Diagrams for Cementitious Waste Stabilization Systems: II, End-Member Stoichiometries of Ideal Calcium Silicate Hydrate Solid Solutions', *Journal of the American Ceramic Society*, vol. 84, no. 12, pp. 3017-3026.

Landgrebe, D & Biehl, L 2001, *An Introduction to Multispec©*, School of Electrical and Computer Engineering, Purdue University, West Lafayette, Indiana. Available from: http://dynamo.ecn.purdue.edu/~biehl/MultiSpec.

Landgrebe, DA 2003, *Signal Theory Methods in Multispectral Remote Sensing*, John Wiley & Sons, Hoboken, NJ.

Lothenbach, B, Le Saout, G, Gallucci, E & Scrivener, K 2008a, 'Influence of limestone on the hydration of Portland cements', *Cement and Concrete Research*, vol. 38, no. 6, pp. 848-860.

Lothenbach, B, Matschei, T, Möschner, G & Glasser, FP 2008b, 'Thermodynamic modelling of the effect of temperature on the hydration and porosity of Portland cement', *Cement and Concrete Research*, vol. 38, no. 1, pp. 1-18.

Lothenbach, B & Wieland, E 2006, 'A thermodynamic approach to the hydration of sulphate-resisting Portland cement', *Waste Management*, vol. 26, no. 7, pp. 706-719.

Lothenbach, B & Winnefeld, F 2006, 'Thermodynamic modelling of the hydration of Portland cement', *Cement and Concrete Research*, vol. 36, no. 2, pp. 209-226.

Martys, N, Bentz, DP & Garboczi, EJ 1994, 'Computer simulation study of the effective viscosity in Brinkman's equation', *Physics of Fluids*, vol. 6, no. 4, pp. 1434-1439.

Martys, NS 2001, 'Improved approximation of the Brinkman equation using a lattice Boltzmann method', *Physics of Fluids*, vol. 13, no. 6, pp. 1807-1810.

Martys, NS & Hagedorn, JG 2002, 'Multiscale modeling of fluid transport in heterogeneous materials using discrete Boltzmann methods', *Materials and Structures*, vol. 35, no. 254, pp. 650-658.

Matschei, T, Lothenbach, B & Glasser, FP 2007, 'Thermodynamic properties of Portland cement hydrates in the system CaO-Al_2O_3-SiO_2-$CaSO_4$-$CaCO_3$-H_2O', *Cement and Concrete Research*, vol. 37, no. 10, pp. 1379-1410.

Parkhurst, DL & Appelo, CAJ 1999, *User's Guide to PHREEQC (Version 2)--A Computer Program for Speciation, Batch-Reaction, One-Dimensional Transport, and Inverse Geochemical Calculations*, Water Resources Investigation Report 99-4259, U.S. Geological Survey, Denver, Colorado.

Parrott, LJ & Killoh, DC 1984, 'Prediction of cement hydration', *Proceedings of the British Ceramic Society*, vol. 35, pp. 41-53.

Promentilla, MAB, Sugiyama, T, Hitomi, T & Takeda, N 2009, 'Quantification of tortuosity in hardened cement pastes using synchrotron-based X-ray computed microtomography', *Cement and Concrete Research*, vol. 39, no. 6, pp. 548-557.

Richardson, IG 2004, 'Tobermorite/jennite- and tobermorite/calcium hydroxide-based models for the structure of C-S-H: applicability to hardened pastes of tricalcium silicate, [beta]-dicalcium silicate, Portland cement, and blends of Portland cement with blast-furnace slag, metakaolin, or silica fume', *Cement and Concrete Research*, vol. 34, no. 9, pp. 1733-1777.

Schwartz, LM, Auzerais, F, Dunsmuir, J, Martys, N, Bentz, DP & Torquato, S 1994, 'Transport and diffusion in three-dimensional composite media', *Physica A: Statistical and Theoretical Physics*, vol. 207, no. 1-3, pp. 28-36.

Stutzman, P 2007, 'Multi-spectral SEM imaging of cementitious materials', in *Proceedings of the Twenty-Ninth Annual Conference on Cement Microscopy*, ed. L Sutter, 20-24 May 2007, Quebec City, Canada.

Stutzman, P & Leigh, S 2007, 'Phase analysis of hydraulic cements by X-ray powder diffraction: precision, bias, and qualification', *J. ASTM International*, vol. 4. Available from: http://www.astm.org/DIGITAL_LIBRARY/JOURNALS/JAI/.

Stutzman, PE & Clifton, JR 1999, 'Sample preparation for scanning electron microscopy', in *Proceedings of the Twenty-First Annual International Conference on Cement Microscopy*, eds L Jany & A Nisperos, 25-29 April 1999, Las Vegas, NV, pp. 10-22.

Sun, Z, Garboczi, EJ & Shah, SP 2007, 'Modeling the elastic properties of concrete composites: Experiment, differential effective medium theory, and numerical simulation', *Cement and Concrete Composites*, vol. 29, no. 1, pp. 22-38.

Taylor, HFW 1997, *Cement Chemistry, 2nd edition*, Thomas Telford, London.

Taylor, MA, Garboczi, EJ, Erdogan, ST & Fowler, DW 2006, 'Some properties of irregular 3-D particles', *Powder Technology*, vol. 162, no. 1, pp. 1-15.

Tomosawa, F 1997, 'Development of a kinetic model for hydration of cement', in *Proceedings of the 10th International congress on the chemistry of cement*, Volume 2, Göteborg, Sweden, pp. 2ii051-2ii058.

U.S. DEPARTMENT OF
ENERGY

VANDERBILT
UNIVERSITY

NIST
National Institute of
Standards and Technology

SIMCO
Technologies inc.